Phosphorene/rhenium disulfide heterojunction-based negative differential resistance device for multi-valued logic

Jaewoo Shim[1], Seyong Oh[1], Dong-Ho Kang[1], Seo-Hyeon Jo[1], Muhammad Hasnain Ali[1], Woo-Young Choi[1], Keun Heo[2], Jaeho Jeon[3], Sungjoo Lee[3], Minwoo Kim[3], Young Jae Song[3] & Jin-Hong Park[1]

Recently, negative differential resistance devices have attracted considerable attention due to their folded current–voltage characteristic, which presents multiple threshold voltage values. Because of this remarkable property, studies associated with the negative differential resistance devices have been explored for realizing multi-valued logic applications. Here we demonstrate a negative differential resistance device based on a phosphorene/rhenium disulfide (BP/ReS$_2$) heterojunction that is formed by type-III broken-gap band alignment, showing high peak-to-valley current ratio values of 4.2 and 6.9 at room temperature and 180 K, respectively. Also, the carrier transport mechanism of the BP/ReS$_2$ negative differential resistance device is investigated in detail by analysing the tunnelling and diffusion currents at various temperatures with the proposed analytic negative differential resistance device model. Finally, we demonstrate a ternary inverter as a multi-valued logic application. This study of a two-dimensional material heterojunction is a step forward toward future multi-valued logic device research.

[1] School of Electronic and Electrical Engineering, Sungkyunkwan University, Suwon 440-746, Korea. [2] Frontier Technology Lab, R&D Headquarters, SK Hynix Co. Ltd., Ichon 460-701, Korea. [3] Sungkyunkwan University Advanced Institute of Nanotechnology, Sungkyunkwan University, Suwon 440-746, Korea. Correspondence and requests for materials should be addressed to J.-H.P. (email: jhpark9@skku.edu).

Recently, negative differential resistance (NDR) devices have attracted considerable attention owing to their folded current–voltage (I–V) characteristic (N-shaped I–V curve), which presents multiple threshold voltage values[1–27]. Because of this remarkable property, studies associated with the NDR devices have been explored for realizing multi-valued logic (MVL) applications[1,7,11,13,26]. Compared to conventional binary logic systems, MVL systems can transmit more information with fewer interconnect lines between devices by transferring multi-valued signals, thereby reducing the complexity of modern integrated circuit design. For example, a ternary logic system is theoretically able to reduce the number of interconnect lines by nearly 45% as compared with binary logic[28]. The NDR devices that have been researched for the implementation of this MVL system are Esaki diodes[2–7], resonant tunnelling diodes[8–20], Gunn diodes, single electron transistors[21,22] and molecular devices[23,24]. However, at the current stage of research, because most of the Esaki diodes and resonant tunnelling diodes were fabricated in Si–Ge and III–V semiconductors[2–4,8–14], the formation of various types of heterojunctions (type-I, II and III) is limited by threading dislocations, which are normally caused at the junction interface by lattice mismatch during film growth. Although the threading dislocation that increases the valley current of NDR device can be reduced by applying superlattice and nanowire structures, it is hard to avoid that the fabrication process becomes more complex.

In this light, atomically thin two-dimensional (2D) semiconductors, such as molybdenum disulfide (MoS_2), tungsten diselenide (WSe_2), rhenium disulfide (ReS_2), tin diselenide ($SnSe_2$) and black phosphorus (BP), are expected to offer attractive material platforms for NDR devices due to the absence of dangling bonds on their surfaces. Because these 2D semiconductor layers are stacked via weak van der Waals interaction, 2D materials-based heterojunctions do not suffer from lattice mismatch and form atomically sharp interfaces, allowing high-quality heterojunction interfaces[29–31]. It is also possible to design various heterojunctions by stacking different 2D materials with different bandgaps and electron affinities, where band structure alignment can be classified into three types: type-I (straddling gap)[32], type-II (staggered gap)[2–4,6,7,33–36] and type-III (broken gap)[5,32]. Recently, Roy et al.[6] reported an NDR device based on an MoS_2/WSe_2 heterostructure, which was fabricated in a type-II heterojunction. However, the NDR device used dual gates involving a complicated fabrication process to obtain an electrostatically doped n^+/p^+ heterojunction, and the NDR behaviour was observed at a very low temperature below 175 K. Nourbakhsh et al. and Yan et al. also reported NDR devices in MoS_2/WSe_2 and $BP/SnSe_2$ heterojunctions, respectively[5,7]. In these devices, it was necessary to use the specific thickness of 2D semiconductors to ensure band-to-band tunnelling of carriers, and the obtained peak-to-valley current ratio (PVCR) values were lower than 2 at room temperature.

Here, we demonstrate an NDR device based on a BP/ReS_2 heterojunction that is formed by type-III broken-gap band alignment, showing high PVCR values of 4.2 and 6.9 at room temperature and 180 K, respectively. In addition, as an MVL application, we present a ternary inverter (having three states) that combines a BP/ReS_2 heterojunction NDR device and a BP p-channel thin film transistor (TFT). This integration approach based on NDR devices is expected to fulfil low-power advantages of future MVL circuits by reducing the parasitic interconnect capacitance. In particular, compared with a type-II heterojunction, a type-III heterojunction can easily implement a highly doped n^+/p^+ heterojunction without a separate process, such as electrostatic doping by gate bias and a chemical doping process. First, we confirm the broken-gap band alignment of the BP/ReS_2

heterojunction with Kelvin probe force microscopy (KPFM). Then, the carrier transport mechanism of the BP/ReS_2 heterojunction NDR device is discussed in detail at room temperature. Furthermore, through temperature-dependent current–voltage (I–V) measurements and the proposed analytic NDR device model, where tunnelling/diffusion currents and parasitic series resistance were considered simultaneously, we quantitatively study the temperature-dependent device operations.

Results

Characteristics of BP/ReS₂ heterostructure. Figure 1a presents schematic diagrams of the BP/ReS_2 heterostructure on an SiO_2/Si substrate. A BP flake was prepared onto an SiO_2/Si substrate by a tape-based exfoliation method[37], and then an ReS_2 flake was transferred onto the BP flake by a mechanical transfer process method (the optical images of the BP/ReS_2 heterostructure can be found in Supplementary Fig. 1)[38]. The thicknesses of the BP and ReS_2 flakes were confirmed by atomic force microscope to be about 40 and 50 nm, respectively (Fig. 1b,c). Figure 1d shows the Raman spectra obtained at three different positions in the BP/ReS_2 heterostructure sample, where the spectra from top to bottom indicate a ReS_2 region, a BP/ReS_2 overlapped region and a BP region. The observed Raman peaks of BP at 366, 442 and 470 cm^{-1} correspond to the A^1_g, B_{2g}, and A^2_g phonon modes, respectively. This Raman spectrum for ReS_2 includes two prominent peaks at 154 and 215 cm^{-1}, which are attributed to the in-plane (E_{2g}) and out-of-plane (A_{1g}) vibrational modes. The Raman spectrum of the overlapped BP/ReS_2 region contains the vibration modes of both BP and ReS_2, indicating the formation of a heterostructure. Next, to investigate the band alignment of the BP/ReS_2 heterojunction, we carried out KPFM measurements. Figure 1e shows the three-dimensional KPFM mapping image of the BP/ReS_2 heterostructure and contact potential difference (ΔV_{CPD}) histograms extracted from the mapping image. Before the KPFM measurement, the KPFM tip (platinum/iridium (Pt/Ir)-coated Si tip) was calibrated on a highly oriented pyrolytic graphite (HOPG) surface. Here, the HOPG is conventionally used to calibrate the work function of the KPFM tip because it has a clean surface and its work function is well known to be 4.6 eV (ref. 39). The average ΔV_{CPD} values on the BP and ReS_2 flakes were obtained at -153 and 430 mV, respectively. Since the ΔV_{CPD} is the difference in the work function between the KPFM tip and the sample (inset of Fig. 1f), the work function values of the BP and ReS_2 can be calculated using the following equation: $\Phi_s = \Phi_{tip} - \Delta V_{CPD}$, where Φ_s and Φ_{tip} are the work functions of the samples (BP and ReS_2) and the KPFM tip, respectively. Here, Φ_{tip} was obtained from the sum of the HOPG work function (Φ_{HOPG}) and ΔV_{CPD} between the KPFM tip and the HOPG surface ($\Phi_{tip} = \Phi_{HOPG} + \Delta V_{CPD\_HOPG}$), which is presented in more detail in Supplementary Fig. 2 (refs 40,41). Therefore, the work function values of the BP and ReS_2 films can be estimated to be about 4.5 and 5.1 eV, respectively (Fig. 1f). Based on the obtained KPFM results and the previously reported band properties (conduction band minimum, valence band maximum and band gap (E_g)) of BP and ReS_2 (refs 42–44), we graphically described the predicted energy band alignment of the BP and ReS_2 heterojunction at equilibrium before contact (Fig. 1g) and after contact (Fig. 1h). Here, the conduction band minimum, valence band maximum and E_g values of the BP (ReS_2) that were calculated using a first-principles density of states in the literature were 4.2 eV (4.68 eV), 4.59 eV (6.05 eV) and 0.39 eV (1.37 eV), respectively. As shown in Fig. 1g, the BP/ReS_2 heterojunction seems to form a broken-gap band alignment (type-III heterojunction) because the highest valence band edge of BP is located above the lowest conduction band edge of ReS_2.
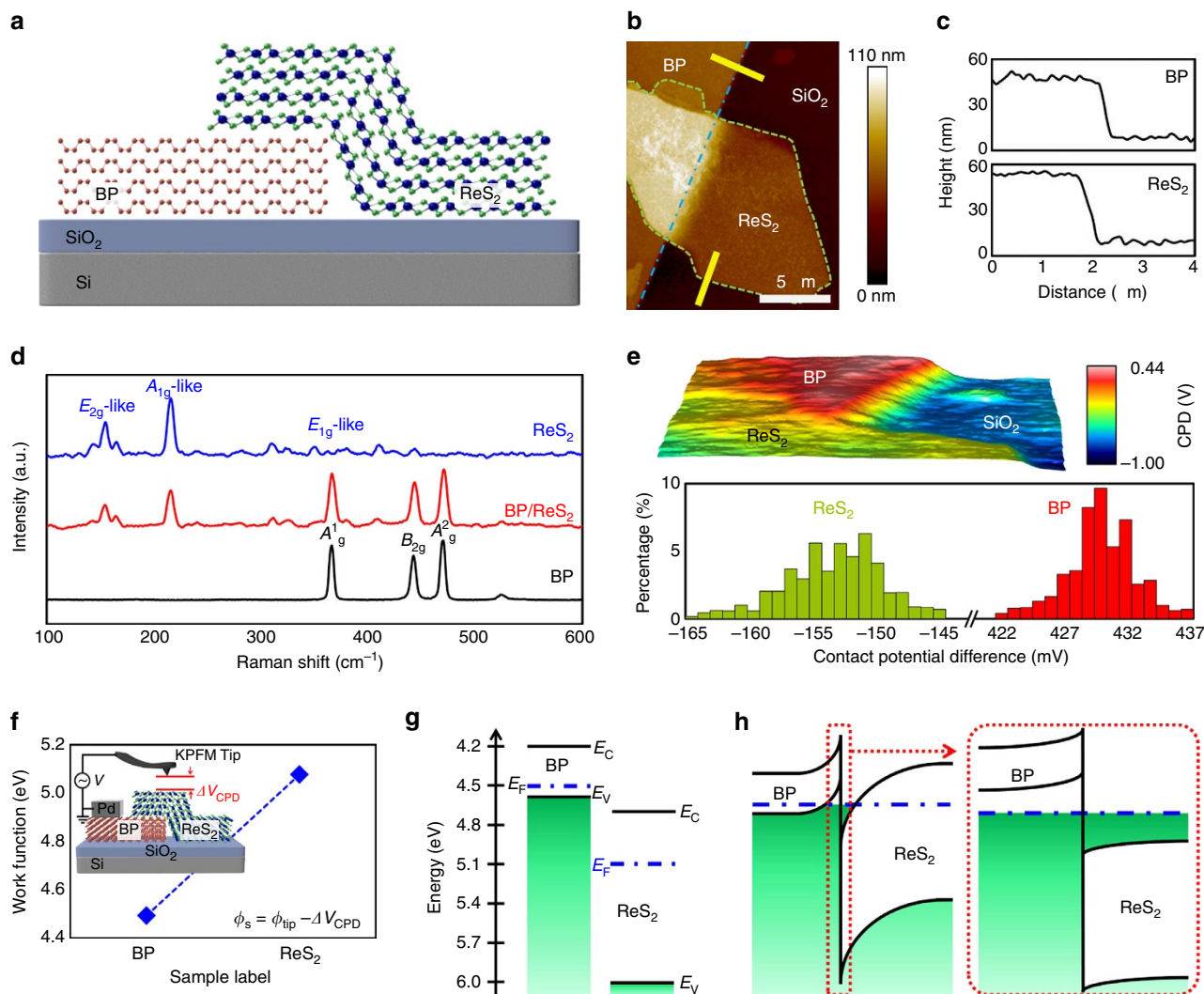
Figure 1 | BP/ReS₂ heterostructure. (**a**) Schematic illustration of the BP/ReS$_2$ heterostructure on SiO$_2$/Si substrate. (**b**) AFM (atomic force microscope) image of the BP/ReS$_2$ heterostructure sample. (**c**) Thicknesses of the BP (top) and the ReS$_2$ flakes (bottom) corresponding to the yellow lines marked in **b**. (**d**) Raman spectra of the ReS$_2$, BP/ReS$_2$ overlapped and BP regions. (**e**) Three-dimensional KPFM mapping image of the BP/ReS$_2$ heterostructure (top) and histogram distributions of ΔV_{CPD} extracted from the KPFM mapping image (bottom). (**f**) Work function values of BP and ReS$_2$ films. The inset shows schematic illustration of the KPFM measurement system. (**g,h**) Energy band alignments of BP and ReS$_2$ heterojunction at equilibrium (**g**) before and (**h**) after contact. E_C, E_F and E_V are the lowest energy level of the conduction band, the Fermi level and the highest energy level of the valence band of the semiconductors, respectively.

Furthermore, owing to the large work function difference (0.6 eV) between BP and ReS$_2$, hole and electron carriers accumulate near the heterojunction interface in BP and ReS$_2$, respectively (Fig. 1h). Therefore, a highly doped n$^+$/p$^+$ heterojunction can easily be implemented by forming a broken-gap band alignment without using a separate doping process, such as electrostatic doping by gate bias or chemical doping, which is generally required in a type-II heterojunction to realize a NDR device[2–4,6,7,33–36].

BP/ReS₂ heterojunction-based NDR device. After fabricating the NDR device based on the BP/ReS$_2$ heterojunction, as shown in Fig. 2a, we performed electrical measurements in the NDR device at room temperature. Figure 2b shows the current–voltage (I–V) characteristic of the NDR device on a linear scale. Here, the NDR behaviour was observed between 0.4 V and 0.9 V with a PVCR of 4.2, which is the highest value in previously reported NDR devices based on 2D materials[5–7,16–19]. We also note that similar electrical characteristics were observed in three different

BP/ReS$_2$ NDR devices with PVCR values between 3.8 and 4.1 (Inset of Fig. 2 and Supplementary Fig. 3). In addition, to understand the operation mechanism of the BP/ReS$_2$ NDR device, we theoretically investigated the current characteristic by considering tunnelling and diffusion currents using a theoretical model that we developed. The equations related to the current transport mechanisms can be found in Supplementary Fig. 4 and the parameters used in the analytic model are tabulated in Supplementary Table 1. The experimentally measured and theoretically calculated I–V curves are shown in Fig. 2c. Under a negative voltage and a positive voltage between 0 and 0.7 V, the tunnelling current seems to dominate the diffusion current, whereas the diffusion current primarily contributes to the operation of the NDR device when a higher voltage is applied (above 0.7 V). This is graphically explained in Fig. 2d, which shows the band alignments of the BP/ReS$_2$ heterojunction under various bias conditions. When a negative voltage is applied ($V < 0$ V), electron carriers are able to tunnel from the filled valence band states in BP to the empty conduction band states in
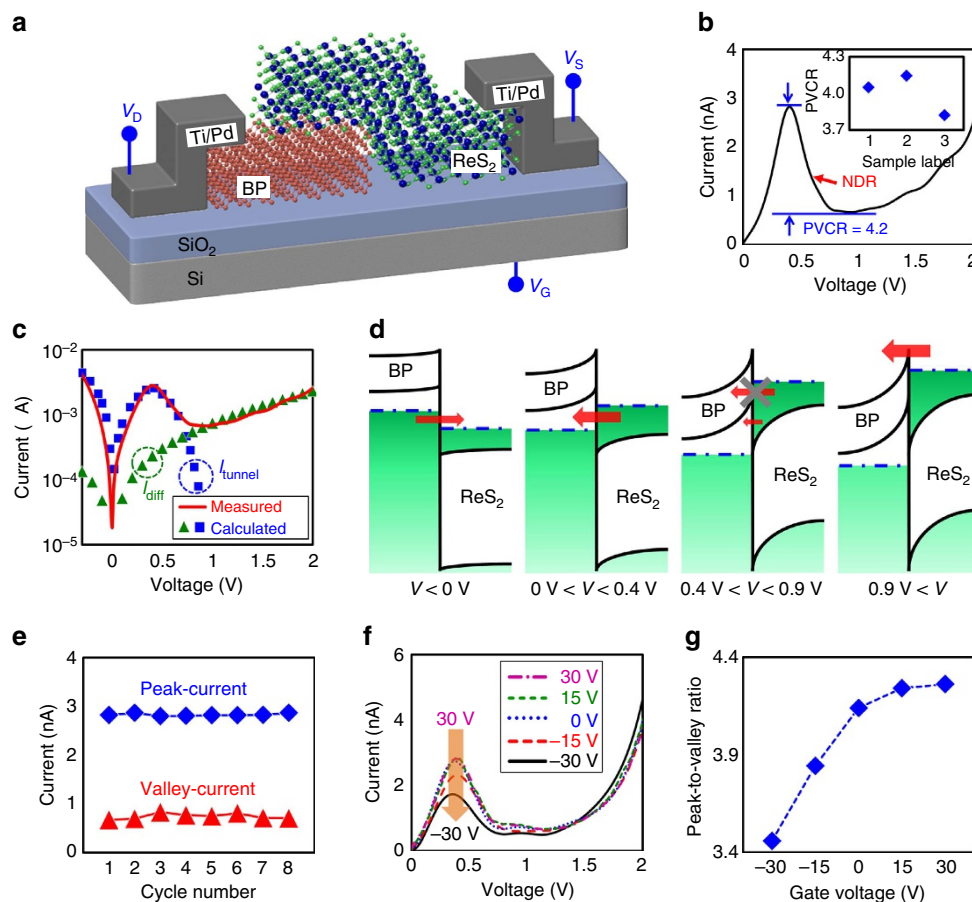
Figure 2 | Electrical characteristics of BP/ReS$_2$ heterojunction-based NDR device at room temperature. (a) An illustration of the BP/ReS$_2$ heterojunction NDR device. **(b)** Current–voltage (I–V) characteristic of the BP/ReS$_2$ NDR device on a linear scale. The inset shows the PVCR values for the three different BP/ReS$_2$ NDR devices. **(c)** Experimentally measured and theoretically calculated I–V curves of the BP/ReS$_2$ NDR device on a log scale. **(d)** Energy band alignment of the BP/ReS$_2$ heterojunction under various bias conditions. Width of the red arrow presents the magnitude of the current. **(e)** Extracted peak- and valley-current values of the BP/ReS$_2$ NDR device in eight consecutive I–V sweeps. **(f)** Drain current–drain voltage (I$_D$–V$_D$) curves under various gate biases from 30 V to −30 V. **(g)** PVCR values of the BP/ReS$_2$ NDR device as a function of gate voltage.

ReS$_2$, consequently increasing the current. Similarly, when a small positive voltage is applied (0 V < V < 0.4 V), the current increases because the electron carriers in the conduction band states of ReS$_2$ are tunnelled into the empty valence band states of BP. This current of the NDR device continuously increases until the Fermi level of ReS$_2$ aligns with the highest valence band energy of BP, where the filled states in the ReS$_2$ are maximally overlapped with unoccupied states of the BP, inducing a maximum tunnelling current (peak current). Further increases in voltage (0.4 V < V < 0.9 V) lead to decreases in the current because the degree of overlap between the filled and empty states is reduced due to the bandgap region. Therefore, the tunnelling current decreases with increasing voltage, and the NDR behaviour is obtained as shown in Fig. 2b,c. When a high voltage is applied (V > 0.9 V), the tunnelling current no longer affects the operation of the NDR device, and the electron carriers are able to diffuse from ReS$_2$ to BP by shrinking the potential hill in the BP/ReS$_2$ heterojunction, consequently again increasing the current of the BP/ReS$_2$ NDR device. Here, the lowest current value that is observed beyond a peak current is called a valley current. We then extracted the peak- and valley-current values of the NDR device for eight consecutive I–V sweeps, where stable peak- and valley-current values were observed, as shown in Fig. 2e. Figure 2f shows the drain current–drain voltage (I$_D$–V$_D$) curves under various gate bias conditions, which also confirms that the peak

current decreases as the gate voltage decreases. When the gate voltage varied from 30 V to −30 V, the Fermi level of BP down-shifted due to the accumulation of hole carriers, which thereby increased the degree of the energy band bending in the BP region (Supplementary Fig. 5). The Fermi level of the stacked ReS$_2$ on the BP is predicted to be barely modulated by an applied gate bias due to the thick BP (strong electrostatic screening effect). The down-shifted energy band in the BP region would form a potential well at the heterojunction interface, where much higher potential barrier height was obtained[45]. This leads to a decrease in the peak current of the BP/ReS$_2$ NDR device with decreasing gate voltage because strongly confined electron carriers in the potential well are difficult to escape from the potential well. The reduction of peak current in BP/ReS$_2$ NDR devices with decreasing gate voltage could also be estimated using the I$_D$–V$_D$ curves calculated by the analytic model (Supplementary Fig. 5). Thus, the PVCR of the BP/ReS$_2$ NDR device was modulated between 4.26 and 3.46 A/A by applying different gate voltages, as shown in Fig. 2g.

Furthermore, to analyse the temperature dependency of the carrier transport in the BP/ReS$_2$ NDR device, we performed I–V measurements at various temperatures between 180 and 300 K. As shown in Fig. 3a, the peak current (I$_{peak}$) increased, whereas the valley current (I$_{valley}$) decreased, with reducing temperature, consequently improving PVCR value from 4.02 to 6.78 A/A
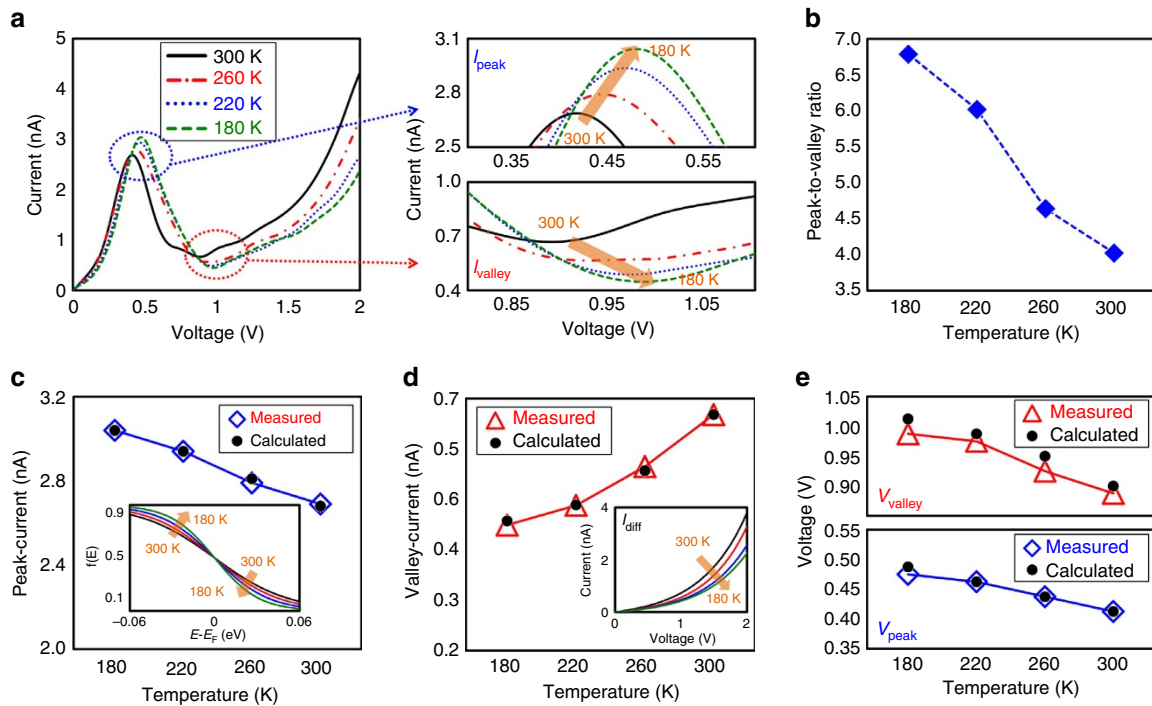
Figure 3 | Temperature-dependent electrical characteristics of BP/ReS$_2$ NDR device. (**a**) I–V curves of the BP/ReS$_2$ NDR device at various temperatures between 180 K and 300 K. (**b**) PVCR values of the BP/ReS$_2$ NDR device as a function of temperature. (**c–e**) Peak-current (**c**), valley-current (**d**), valley- and peak-voltage values of the BP/ReS$_2$ NDR device as a function of temperature (**e**), which were extracted from the experimentally measured and the theoretically calculated I–V characteristic curves. The inset in **c** shows the probability of states being occupied (f(E)) as a function of given energy E relative to E_F($E - E_F$). The inset in **d** shows the theoretically calculated diffusion current of the BP/ReS$_2$ NDR device at various temperatures.

(Fig. 3b). In addition, the peak-voltage (V_{peak}) and valley-voltage (V_{valley}) values shifted positively as the measurement temperature was reduced. To quantitatively analyse the temperature-dependent electrical characteristics of the BP/ReS$_2$ NDR device, we exploited the proposed analytic NDR device model. The calculated I–V characteristic curves at different temperatures are presented in Supplementary Fig. 6, where the I–V curves estimated by the analytic model were well fitted with the measured I–V data. Figure 3c shows the I_{peak} data as a function of temperature, which were extracted from the experimentally measured and the theoretically calculated I–V characteristics. Because a large portion of I_{peak} is mainly occupied by I_{tunnel}, as shown in Fig. 2c, the I_{peak} seems to be associated with the density of states in the conduction band of ReS$_2$ and the valence band of BP, where the density of occupied or empty states is determined by the Fermi–Dirac function. Thus, we focused on an analysis on the temperature dependency of the Fermi–Dirac distribution. As the temperature decreases, the Fermi–Dirac distribution near the Fermi level of BP and ReS$_2$ becomes sharp, thereby increasing the probability of states being occupied (f(E)) in the conduction band of ReS$_2$, as shown in the inset of Fig. 3c, where f(E) at energy E of $E_F - 0.03$ eV were 0.76 and 0.87 at 300 K and 180 K, respectively. Meanwhile, the f(E) in the valence band of BP decreases (thereby, an increase in probability of states being empty) with reducing the temperature, where f(E) at energy $E = E_F + 0.03$ eV were 0.24 and 0.13 at 300 and 180 K, respectively. This subsequently increases I_{tunnel} because of the increased occupied states in conduction band of ReS$_2$ and the decreased empty states in valence band of BP, eventually resulting in a slight increase of I_{peak} (2.7 nA at 300 K and 3.0 nA at 180 K in Fig. 3c). In contrast, because the dominant current of I_{valley} is I_{diff}, which is dependent on temperature (see the inset of Fig. 3d), I_{valley} is predicted to reduce with decreasing temperature (0.67 nA at 300 K and

0.45 nA at 180 K, in Fig. 3d). Overall, in the BP/ReS$_2$ NDR device, the temperature dependencies of I_{peak} and I_{valley} were differently presented due to the increase in I_{tunnel} and the decrease in I_{diff} as the measurement temperature decreased. Meanwhile, we also considered parasitic series resistance (R_s) in the analytic model to accurately analyse the device operation. R_s is mainly associated with the contact resistance between the metal electrode and the semiconductor[46]. Here, the reduction in n-type carrier concentration due to decreasing temperature leads to an increase in the depletion width at the metal/semiconductor (MS) junction and thereby a suppression of the e-field-dependent barrier height lowering effect, eventually increasing the contact resistance at the MS junction (Supplementary Fig. 7)[47]. Thus, as shown in Fig. 3e, positively shifted V_{peak} and V_{valley} were observed as measurement temperature decreased because a higher voltage was required to operate the NDR device due to the increased R_S at reduced temperature.

Ternary inverter with three logical states. Finally, we fabricated a ternary inverter, which is a basic building block in MVL applications, as schematically shown in Fig. 4a. This ternary inverter was formed by integrating the BP/ReS$_2$ heterojunction NDR device as a driver with the built-in BP p-channel TFT as a load resistor, where the total resistance in the BP TFT could be controlled by an applied gate voltage (Supplementary Fig. 8). Figure 4b,c show the equivalent circuit configuration and an optical image of the ternary inverter, respectively. The supply (V_{DD}) and input voltages (V_{IN}) were applied to the source electrode on the BP and the back gate. The metal electrode on the ReS$_2$ (source electrode in the BP/ReS$_2$ NDR device) was connected to the ground (V_{SS}), and then we measured the output voltage (V_{OUT}) on the middle shared electrode (drain electrode in
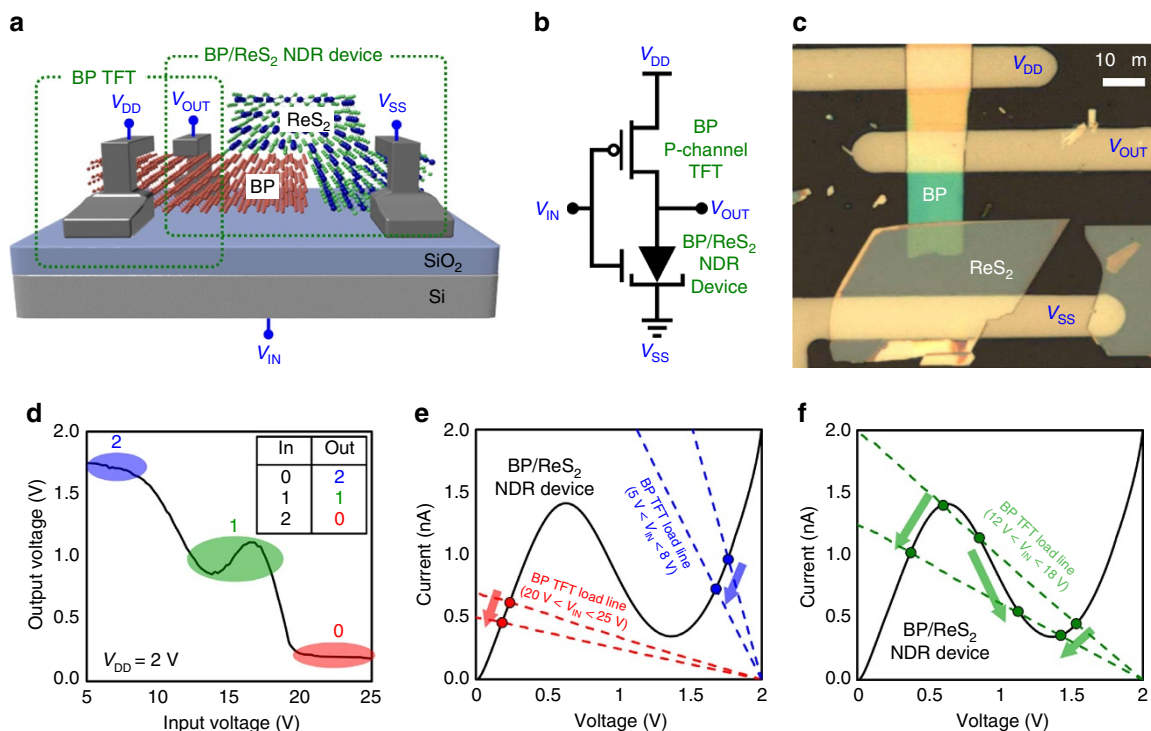
Figure 4 | Ternary inverter with three logical states. (**a**) Schematic illustration of the ternary inverter. (**b**) Equivalent circuit configuration of the ternary inverter. (**c**) Optical image of the ternary inverter. (**d**) V_{IN} versus V_{OUT} characteristic of the ternary inverter. The inset shows an input–output table of the ternary inverter. (**e,f**) Load-line analysis of the ternary inverter circuit under three bias conditions: (**e**) 5 V < V_{IN} < 8 V, 20 V < V_{IN} < 25 V and (**f**) 12 V < V_{IN} < 18 V. The I–V characteristics of the BP/ReS$_2$ NDR device (driver) and the BP TFT (load resistor) are represented by solid and dashed lines, respectively.

the BP TFT and in the BP/ReS$_2$ NDR device). The V_{IN} versus V_{OUT} characteristic of the ternary inverter is shown in Fig. 4d, where V_{DD} was 2 V. When V_{IN} varied from 5 V to 25 V, V_{OUT} showed three distinct states: (i) V_{OUT} > 1.7 V (state '2') for 5 V < V_{IN} < 8 V, (ii) 0.85 V < V_{OUT} < 1.12 V (state '1') for 12 V < V_{IN} < 18 V and (iii) V_{OUT} < 0.24 V (state '0') for 20 V < V_{IN} < 25 V. To explain the operation of this ternary inverter, we performed a load-line circuit analysis, in which the intersections of the two characteristic curves indicate the operating points of this circuit. As shown in Fig. 4e, when a low V_{IN} is applied (5 V < V_{IN} < 8 V), the load resistor (BP TFT) provides a low-resistance path between the source (V_{DD}) and drain (output) nodes of the BP TFT because the applied V_{IN} is higher than the threshold voltage (V_{TH}) of the BP TFT (Supplementary Fig. 8). Thus, high voltage values (logic state '2'), which were close to V_{DD}, were measured at the output terminal (blue circles in Fig. 4e). In contrast, when a high V_{IN} was applied (20 V < V_{IN} < 25 V), the BP TFT was turned off (V_{IN} < V_{TH}), which creates a low-resistance path between the output terminal and the ground. This consequently presented low voltage values (logic state '0') at the output terminal (red circles in Fig. 4e). When a moderate V_{IN} was applied (12 V < V_{IN} < 18 V), the operating points were located at the NDR region in the I–V curve of the BP/ReS$_2$ NDR device, as shown in Fig. 4f. This resulted in intermediate output values (logic state '1') with small fluctuations due to an imbalance of the operating points, where the three intersections were. Overall, by integrating the BP/ReS$_2$ NDR device with the built-in BP TFT, the ternary inverter was simply demonstrated as an MVL application.

Discussion

We demonstrated a NDR device based on a BP/ReS$_2$ heterojunction with high PVCR values of 4.2 and 6.8 at room temperature

and 180 K, respectively. This NDR characteristic can be easily achieved by forming a broken-gap (type-III) band alignment without a separate process, such as electrostatic doping by gate bias and a chemical doping process, which is generally required in type-II heterojunction to realize an NDR device. The broken-gap band alignment of the BP/ReS$_2$ heterojunction was confirmed through KPFM measurements, where the band gaps of the BP and ReS$_2$ did not overlap at all (type-III). Also, the carrier transport mechanisms of the BP/ReS$_2$ NDR device were investigated in detail by analysing the tunnelling and diffusion currents at various temperatures between 180 and 300 K by using the proposed analytic NDR device model. Specifically, we confirmed that I_{peak} increased while I_{valley} decreased as the measurement temperature was reduced, consequently providing a PVCR value that improved from 4.02 to 6.8. Finally, we demonstrated a ternary inverter as an MVL application, which was fabricated by integrating a BP/ReS$_2$ heterojunction NDR device with a built-in BP TFT. In the V_{IN} versus V_{OUT} characteristic of the ternary inverter, when V_{IN} varied from 5 to 25 V, V_{OUT} showed three distinct values (states '2', '1' and '0'). This study of a 2D material heterojunction is a step forward toward future multi-valued logic device research.

Methods

Fabrication of the BP/ReS$_2$ heterojunction-based NDR devices. A BP flake was exfoliated onto a 90 nm thick SiO$_2$/Si substrate by adhesive tape (224SPV, Nitto). Then, a ReS$_2$ flake was transferred onto the BP flake by using a mechanical transfer process method. Finally, the source and drain electrode regions were patterned by optical lithography, and Ti/Pd (10/30 nm) layers were deposited on an electron-beam evaporating system, followed by a lift-off process.

Fabrication of the ternary inverter. By using a mechanical transfer method, a ReS$_2$ flake was stacked onto the BP flake, which was exfoliated onto a 90 nm thick SiO$_2$/Si substrate. The metal electrode regions were defined using a conventional photolithography process. Finally, Ti/Pd (10/30 nm) layers were deposited by

e-beam evaporation to form the contacts for BP and ReS_2, followed by a lift-off process in acetone. The BP/ReS_2 NDR and the BP TFT devices were designed to function as a driver and a load resistor for a ternary inverter, respectively. The voltage of V_{DD} was applied to the source electrode of the BP TFT, and the source electrode of the BP/ReS_2 NDR device was connected to the ground (V_{SS}). The common back gate of the BP TFT and BP/ReS_2 NDR devices served as the input voltage (V_{IN}) electrode. The output voltage (V_{OUT}) was measured at the drain electrode of the BP/ReS_2 NDR device.

Characterization of the BP/ReS_2 heterojunctions. Raman studies were conducted using a WITec micro-Raman spectrometer system with a frequency-doubled Nd-YAG laser beam (532 nm laser excitation). The atomic force microscope analysis was carried out in an XE 100 (Park Systems Corp.) system. The electrical transport measurements were conducted at room temperature under ambient conditions in a probe station with a Keysight B2912A. The temperature-dependent electrical characteristics were measured in a vacuum chamber (below 10^{-4} Torr) using a Keithley 4200 Semiconductor Parameter Analyzer. The KPFM measurement was performed using NTEGRA Spectra (NT-MDT).

Theoretic model of carrier transport in BP/ReS_2 heterojunctions. The tunnelling current (I_{tunnel}) and diffusion current (I_{diff}) were considered to understand the operating mechanism of the BP/ReS_2 NDR device. The I_{tunnel} can be obtained from

$$I_{tunnel} = \frac{2\pi\alpha q}{h} \int_{E_{C\_Re}}^{E_{V\_BP}} DOS_{BP}(E) \times DOS_{Re}(E) \times [f_{BP}(E) - f_{Re}(E - q(V - IR_s))]dE \tag{1}$$

where α is the screening factor, q is the elementary charge, h is the Planck constant, E_{V_BP} is the highest valence band energy in BP, E_{C_Re} is the lowest conduction band energy in ReS_2. $DOS_{BP}(E)$, $DOS_{Re}(E)$, $f_{BP}(E)$ and $f_{Re}(E)$ mean the density of states and Fermi–Dirac distribution functions of BP and ReS_2, respectively.

The I_{diff} is obtained from

$$I_{diff} = qI_0\left[\exp\left(\frac{V - IR_s}{\eta_{id}k_B T}\right) - 1\right] \tag{2}$$

where I_0 is the saturation current, V is the applied voltage, I is the junction current, R_s is the series resistance, η_{id} is the ideality factor, k_B is the Boltzmann constant and T is the temperature.

Data availability. The data that support the findings of this study are available from the corresponding author upon request.

References

1. Gan, K.-J., Tsai, C.-S., Chen, Y.-W. & Yeh, W.-K. Voltage-controlled multiple-valued logic design using negative differential resistance devices. *Solid State Electron.* **54,** 1637–1640 (2010).
2. Ganjipour, B. *et al.* High current density Esaki tunnel diodes based on GaSb-InAsSb heterostructure nanowires. *Nano Lett.* **11,** 4222–4226 (2011).
3. Desplanque, L. *et al.* Influence of nanoscale faceting on the tunneling properties of near broken gap InAs/AlGaSb heterojunctions grown by selective area epitaxy. *Nanotechnology* **25,** 465302 (2014).
4. Li, Q., Han, Y., Lu, X. & Lau, K. M. GaAs-InGaAs-GaAs fin-array tunnel diodes on (001) Si substrates with room-temperature peak-to-valley current ratio of 5.4. *IEEE Electron Dev. Lett.* **37,** 24–27 (2016).
5. Yan, R. *et al.* Esaki diodes in van der Waals heterojunctions with broken-gap energy band alignment. *Nano Lett.* **15,** 5791–5798 (2015).
6. Roy, T. *et al.* Dual-gated MoS_2/WSe_2 van der Waals tunnel diodes and transistors. *ACS Nano* **9,** 2071–2079 (2015).
7. Nourbakhsh, A., Zubair, A., Dresselhaus, M. S. & Palacios, T. Transport properties of a MoS_2/WSe_2 heterojunction transistor and its potential for application. *Nano Lett.* **16,** 1359–1366 (2016).
8. Schmidt, O. G. *et al.* Resonant tunneling diodes made up of stacked self-assembled Ge/Si islands. *Appl. Phys. Lett.* **77,** 4341–4343 (2000).
9. Duschl, R. & Eberl, K. Physics and applications of Si/SiGe/Si resonant interband tunneling diodes. *Thin Solid Films* **380,** 151–153 (2000).
10. See, P. & Paul, D. J. The scaled performance of Si/Si1-xGex resonant tunneling diodes. *IEEE Electron Dev. Lett.* **22,** 582–584 (2001).
11. Jin, N. *et al.* Tri-state logic using vertically integrated Si–SiGe resonant interband tunneling diodes with double NDR. *IEEE Electron Dev. Lett.* **25,** 646–648 (2004).
12. Brown, E. R. *et al.* Oscillations up to 712 GHz in InAs/AlSb resonant-tunneling diodes. *Appl. Phys. Lett.* **58,** 2291–2293 (1991).
13. Waho, T., Chen, K. J. & Yamamoto, M. Resonant-tunneling diode and HEMT logic circuits with multiple thresholds and multilevel output. *IEEE J. Solid State Circuits* **33,** 268–274 (1998).
14. Nakamura, M., Takahagi, S., Saito, M. & Suhara, M. Analysis of a monolithic integrated rectenna by using an InGaAs/InAlAs triple-barrier resonant tunneling diode for zero bias detection of submilimeter-waves. *Phys. Status Solidi C* **9,** 377–380 (2012).
15. Fallahazad, B. *et al.* Gate-tunable resonant tunneling in double bilayer graphene heterostructures. *Nano Lett.* **15,** 428–433 (2015).
16. Britnell, L. *et al.* Resonant tunnelling and negative differential conductance in graphene heterostructures. *Nat. Commun* **4,** 1794 (2013).
17. Mishchenko, A. *et al.* Twist-controlled resonant tunnelling in graphene/boron nitride/graphene heterostructures. *Nat. Nanotechnol* **9,** 808–813 (2014).
18. Nguyen, L.-N. *et al.* Resonant tunneling through discrete quantum states in stacked atomic-layered MoS_2. *Nano Lett.* **14,** 2381–2386 (2014).
19. Lin, Y.-C. *et al.* Atomically thin resonant tunnel diodes built from synthetic van der Waals heterostructures. *Nat. Commun.* **6,** 7311 (2015).
20. Buchs, G., Ruffieux, P., Gröning, P. & Gröning, O. Defect-induced negative differential resistance in single-walled carbon nanotubes. *Appl. Phys. Lett.* **93,** 073115 (2008).
21. Heij, C. P., Dixon, D. C., Hadley, P. & Mooij, J. E. Negative differential resistance due to single-electron switching. *Appl. Phys. Lett.* **74,** 1042–1044 (1999).
22. Simonian, N., Li, J. & Likharev, K. Negative differential resistance at sequential single-electron tunnelling through atoms and molecules. *Nanotechnology* **18,** 424006 (2007).
23. Chen, J., Reed, M. A., Rawlett, A. M. & Tour, J. M. Large on-off ratios and negative differential resistance in a molecular electronic device. *Science* **286,** 1550–1552 (1999).
24. Mentovich, E. D. *et al.* Multipeak negative-differential-resistance molecular device. *Small* **4,** 55–58 (2008).
25. Wu, Y. *et al.* Three-terminal graphene negative differential resistance devices. *ACS Nano* **6,** 2610–2616 (2012).
26. Liu, G., Ahsan, S., Khitun, A. G., Lake, R. K. & Balandin, A. A. Graphene-based non-Boolean logic circuits. *J. Appl. Phys.* **114,** 154310 (2013).
27. Sharma, P., Bernard, L. S., Bazigos, A., Magrez, A. & Ionescu, A. M. Room-temperature negative differential resistance in graphene field effect transistors: experiments and theory. *ACS Nano* **9,** 620–625 (2015).
28. Hurst, S. L. Multiple-valued logic-its status and its future. *IEEE Trans. Comp.* **c-33,** 1160–1179 (1984).
29. Wang, L. *et al.* One-dimensional electrical contact to a two-dimensional material. *Science* **342,** 614–617 (2013).
30. Jo, S.-H. *et al.* A high-performance WSe_2/h-BN photodetector using a triphenylphosphine (PPh3)-based n-doping technique. *Adv. Mater.* **28,** 4824–4831 (2016).
31. Shim, J. & Park, J.-H. Optimization of graphene-MoS_2 barristor by 3-aminopropyltriethoxysilane (APTES). *Org. Electron* **33,** 172–177 (2016).
32. Zhang, J., Zhang, M., Sun, R.-Q. & Wang, X. A facile band alignment of polymeric carbon nitride semiconductors to construct isotype heterojunctions. *Angew. Chem. Int. Ed.* **124,** 10292–10296 (2012).
33. Lee, C.-H. *et al.* Atomically thin p–n junctions with van der Waals heterointerfaces. *Nat. Nanotechnol.* **9,** 676–681 (2014).
34. Fang, H. *et al.* Strong interlayer coupling in van der Waals heterostructures built from single-layer chalcogenides. *Proc. Natl Acad. Sci. USA* **111,** 6198–6202 (2014).
35. Furchi, M. M. *et al.* Photovoltaic effect in an electrically tunable van der Waals heterojunction. *Nano Lett.* **14,** 4785–4791 (2014).
36. Hong, X. *et al.* Ultrafast charge transfer in atomically thin MoS_2/WS_2 heterostructures. *Nat. Nanotechnol.* **9,** 682–686 (2014).
37. Kang, D.-H. *et al.* An ultrahigh-performance photodetector based on a perovskite–transition-metal-dichalcogenide hybrid structure. *Adv. Mater.* **28,** 7799–7806 (2016).
38. Shim, J. *et al.* Extremely large gate modulation in vertical graphene/WSe_2 heterojunction barristor based on a novel transport mechanism. *Adv. Mater.* **28,** 5293–5299 (2016).
39. Takahashi, T., Tokailin, H. & Sagawa, T. Angle-resolved ultraviolet photoelectron spectroscopy of the unoccupied band structure of graphite. *Phys. Rev. B* **32,** 8317–8324 (1985).
40. Shim, J. *et al.* High-performance 2D rhenium disulfide (ReS_2) transistors and photodetectors by oxygen plasma treatment. *Adv. Mater.* **28,** 6985–6992 (2016).
41. Jo, S.-H. *et al.* Broad detection range rhenium diselenide photodetector enhanced by (3-aminopropyl)triethoxysilane and triphenylphosphine treatment. *Adv. Mater.* **28,** 6711–6718 (2016).
42. Perello, D. J., Chae, S. H., Song, S. & Lee, Y. H. High-performance n-type black phosphorus transistors with type control via thickness and contact-metal engineering. *Nat. Commun.* **6,** 7809 (2015).
43. Liu, X. *et al.* Black phosphorus based field effect transistors with simultaneously achieved near ideal subthreshold swing and high hole mobility at room temperature. *Sci. Rep.* **6,** 24920 (2016).

44. Ho, C. H., Huang, Y. S., Chen, J. L., Dann, T. E. & Tiong, K. K. Electronic structure of ReS$_2$ and ReSe$_2$ from first-principles calculations, photoelectron spectroscopy, and electrolyte electroreflectance. *Phys. Rev. B* **60,** 15766–15771 (1999).
45. Mikhailova, M. P., Moiseev, K. D. & Yakovlev, Y. P. Interface-induced optical and transport phenomena in type II broken-gap single heterojunctions. *Semicond. Sci. Technol.* **19,** R109–R128 (2004).
46. Zhou, P. *et al.* Low series resistance high-efficiency GaAs/AlGaAs vertical-cavity surface-emitting lasers with continuously graded mirrors grown by MOCVD. *IEEE Photonics Technol. Lett* **3,** 591–593 (1991).
47. Rideout, V. L. A review of the theory, technology and applications of metal-semiconductor rectifiers. *Thin Solid Films* **48,** 261–291 (1978).

Acknowledgements

Author contributions

J.S. and J.-H.P. conceived and designed the experiments. J.S., S.O., D.-H.K., S.-H.J., M.H.A., W.-Y.C. and K.H. contributed to the experimental design and device fabrication. J.S. analysed the data and performed the theoretical calculations. J.J. and S.L. conducted the Raman study and data analysis. M.K. and Y.J.S. performed the KPFM measurement. J.-H.P. supervised the research. All the authors discussed the results and commented on the manuscript.

Additional information